Influence of dispersoids on microstructure evolution and work hardening behavior of aluminum alloys during tension and cold rolling

Qinglong Zhao[a], Bjørn Holmedal[a], Yanjun Li[b]

[a] Department of Materials Science and Engineering, Norwegian University of Science and Technology, Trondheim N-7491, Norway

[b] SINTEF Materials and Chemistry, Trondheim N-7465, Norway

Abstract: The influence of dispersoids on work hardening behavior of aluminum during tension and cold rolling has been studied by comparing Al-Mn alloys containing similar amounts of solutes but various dispersoid densities. The microstructure evolution with deformation strain was examined in both transmission and scanning electron microscopy. It is found that a high density of fine dispersoids strengthens the materials significantly, but their strengthening effect diminishes as the strain increases. From a series of Bauschinger tests, it is found that the internal stress due to particles increases rapidly at the initial stage of deformation, but it saturates at strains larger than 5%. It is concluded that the internal stress make a small contribution to the work hardening and contributes to less than 10% of the total flow stress during monotonic loading at strains larger than 5%. The work hardening behavior has been correlated to the corresponding microstructure and the strengthening mechanism is discussed.

Key words: aluminum alloys; mechanical characterization; strain hardening;

1. Introduction

Dispersion hardening caused by non-shearable particles is an important mechanism to strengthen materials. While precipitates are the essential strengthening phase in heat-treatable alloys, the dispersoids precipitated in non-heat-treatable aluminum alloys usually have a smaller contribution to the strength, due to their relatively low number density and large size. Still the dispersoids can have a considerable influence on the strengthening of the non-heat-treatable alloys. Recently it is reported that by optimizing the heat treatment, dispersoids of high density and small size can be achieved in 3xxx aluminum alloys, which can significantly increase the strength of the alloy [1].

Dispersoids also affect work hardening behavior of metals. Early research works have reported the work hardening behavior of dispersion-hardened copper crystals during tensile tests and the corresponding dislocation structure [2-5]. It was found that a small volume fraction of dispersoids in pure copper single crystals resulted in a parabolic work hardening behavior at small strains,

which was different from the linear work hardening in single crystals without dispersoids [2]. At larger tensile strains, the crystal showed a work hardening similar to the matrix material when the volume fraction of dispersoids was small [2]. Similar effect of dispersoids on work hardening during tension tests is also found in aluminum alloys [6-7]. A cross-over effect in stress-strain curves of an AA3207 alloy with and without dispersoids was observed [8]. It shows that in stage III the work hardening rate of the alloy with dispersoids decreased more rapidly than the alloy without dispersoids [8]. A similar effect was also observed in an AA6111 alloy with varied Fe and Mn levels [7], but the particles were not characterized. Only a few studies have considered the work hardening behavior of aluminum alloys containing dispersoids at large strains [9-10]. Research on a cold rolled aluminum containing 4% nano-size alumina particles showed that the strength of the alloy reached a maximum at a strain of ~1, and decreased slightly with further increased strain [9-10].

TEM investigations [3, 5, 11] show that dislocation loops form around dispersoids as Orowan loops or prismatic loops during deformation, resulting in a high dislocation density. These dislocation loops are often referred as geometrically necessary dislocations (GNDs), and can be converted to helices or dipoles [5]. A high density of dispersoids enhances the tendency for dislocations to arrange into a cell structure [9-10], leading to a reduced cell size compared to single-phase materials [3, 9, 12].

The effect of dispersoids on the yield strength is generally explained by the well-known Orowan bypass mechanism, as reviewed by several authors [13-15]. However, the influence of dispersoids on work hardening can not be explained by any single mechanism. In the literature it has been explained by either long-range internal stress or short-range dislocation interactions. Fisher et al. [16] first proposed that the work hardening of dispersion-hardened metals was attributed to the long-range internal stress due to the dislocation loops around dispersoids. Later Brown and Stobbs [17-18] established a theory of work hardening based on internal stress using elastic continuum mechanics. Ashby [2, 19] proposed a model of work hardening based on the short-range interactions between gliding dislocations and GNDs. Hirsh and Humphreys [4] proposed a similar model as Ashby's to explain the work hardening of dispersion-hardened single crystals of copper alloys. Recent research on aluminum alloys containing precipitates or dispersoids agrees that both internal stress and dislocation interactions contribute to the work hardening [20-21].

In previous experimental studies [8-10] the alloy with dispersoids has been compared to alloys without dispersoids but also probably with different levels of solutes. This difference in the solute content made it difficult to directly conclude the influence of dispersoids on work hardening

behavior. Furthermore, very few experimental results have been reported on dispersion hardened materials deformed more than what can be achieved by tensile tests. In order to reveal solely the dispersoid influence on work hardening behavior, the solute content needs to be well controlled. In the present work, a set of carefully designed heat treatments are carried out to generate the same solid solution levels and different number densities of dispersoids in a model Al-Mn alloy. The influence of dispersoids on strengthening and work hardening behavior at moderate and large strains is investigated.

2. Experimental

The material used in this study was an Al-Mn-Fe-Si direct chill cast billet with a diameter of 228 mm produced by Hydro Aluminum, following the standard casting practice with respect to grain refiner addition and casting speed. The chemical composition of the alloy (wt %) was: Mn 0.97, Fe 0.50, Si 0.15 and others 0.05. Samples for cold rolling and tensile tests were cut from the half radius location of the ingot. The average grain size and secondary dendrite arm spacing of the as-cast alloy were measured as 103.6 and 28.2 μm, respectively, by using a lineal intercept procedure with optical microscope. Homogenization heat treatment was conducted in an air circulation furnace. Four different homogenization procedures were designed to obtain two different solute levels and for each of the solute levels to obtain two different size distributions of dispersoids. The detailed homogenization procedures are listed in Table 1. The labels “A” and “B” represent the solid solution levels of Mn in the alloy, while the labels “H” and “L” represent high and low number densities of dispersoids, respectively in the as-homogenized materials. Electrical conductivity of as-homogenized materials was measured by using a Foerster Sigmatest 2.069 to evaluate the solid solution level of Mn. The solid solution levels of different alloying elements of BH and BL were also measured by thermoelectric power (TEP) at Hydro Aluminum Deutschland GmbH R&D center, Bonn.

Table 1 Homogenization treatments

	Homogenization before water quenching
AH	50K/h from room temperature (RT) to 823K
AL	50K/h from RT to 873K, held 8h
BH	50K/h from RT to 723K, held 4h
BL	50K/h from RT to 873K, held 4h + 25°C/h to 773K held 4h

After homogenization, samples BH and BL were rolled at room temperature in a laboratory mill down to about 1.5mm in thickness to achieve von Mises strains of 0.74, 1.8, and 3.3 (nominal reduction 50%, 80%, and 95% respectively). The samples AH and AL were rolled with reductions of 30%, 50% and 80%.

The microstructure of the alloy after homogenization and tension testing to the strain of 0.16 was observed by a JEOL 2010 transmission electron microscope (TEM) at 200KV. The TEM foils were cut from the cross section plane of the deformed specimens. TEM foils were prepared by twin-jet electropolishing in an electrolyte containing two parts methanol and one part nitric acid at 253K and 20V. The as-homogenized microstructure and deformation structure after rolling were observed by backscattered electron channeling contrast (BSE-ECC) imaging at 15KV in a Zeiss Ultra 55 field emission gun scanning electron microscope (SEM).

Tensile testing of the homogenized materials was performed using cylindrical specimens with a diameter of 6mm. The rolled specimens for tensile tests were 6 mm wide and 1.5 mm thick. The extensometer gauge length was 25 mm. An MTS 810 hydraulic testing machine was applied for tensile tests under a constant ramp rate at room temperature, giving a strain rate of $\sim 10^{-3}\ s^{-1}$. The specimens for the Bauschinger tests were of 7 mm in diameter and their parallel length was 20 mm. The extensometer gauge length was 10 mm. The tests were carried out first in tension and then in compression, or in the opposite order. The strain rate was $\sim 10^{-4} s^{-1}$. Most of the investigations were carried out on BH and BL. Samples AH and AL were used to verify some experimental results of BH and BL.

3. Results

3.1 As-homogenized microstructure

The measured values of the electrical conductivity of the as-homogenized materials are shown in Table 2. AH and AL have nearly the same electrical conductivity. That is also the case for BH and BL. It implies that AH has similar solute concentration to AL while BH and BL have about the same solute level. A further quantitative evaluation on the Mn contents in solid solution can be done based on the relationship between the electrical conductivity (EC) and the concentration of alloying elements in solid solution, which is adapted from Ref. [22]:

$$1/EC = 0.0267 + 0.032\ Fe\% + 0.033\ Mn\% + 0.0068\ Si\% + 0.0021\ Particle\%, \quad (1)$$

where Fe%, Mn%, Si% are the weight percentages of the amounts of these elements in solid solution, and Particle% is the total volume fraction of particles. Since the concentration of Si in solid solution was very small (the Si% values measured by TEP were in the range of 0.01~0.02wt% in BH and BL), it influences the electrical conductivity much less than Fe and Mn. Thus, the Si% was set to be constant, 0.01wt% in the calculation. The concentration of Fe in solid solution is very small due to its low solubility and is therefore negligible. Then the Mn content in solution could be calculated from the electrical conductivity. The results are listed in Table 2. As can be seen, two

levels of solutes in solid solution, a high level of Mn in AH and AL compared to a low level in BH and BL has been achieved.

Table 2 The electrical conductivity (EC), concentrations of solutes, the diameters and fractions of particles.

	EC, MS/m	Mn, wt%	Constituent particles		Dispersoids		
			Diameter, μm	Area fraction	Diameter, μm	Volume fraction	Spacing, μm
AH	21.3	0.39	1.4	3.1%	0.09	0.32%	1.08
AL	21.3	0.38	1.6	3.5%	0.12	0.16%	1.53
BH	24.0	0.25	1.0	2.4%	0.11	0.81%	0.85
BL	23.8	0.26	1.5	2.8%	0.16	0.41%	1.37

The morphology and distribution of the constituent particles in BH and BL are shown in Figure 1. The constituent particles in BL were coarser than those in BH, which is due to the coarsening of particles during long time homogenization at a higher temperature. A detailed study on the evolution of constituent particles in a similar alloy during homogenization can be found in Ref. [23]. The diameter and area fraction of constituent particles and dispersoids have been measured by a quantitative image analysis of SEM images and the results are shown in Table 2. It should be noted that the observed surface was not ideal two-dimensional section since the coarse particles are protruded out of the surface section. Thus, the measured area fraction of coarse constituent particles is larger than the volume fraction. α-Al(Mn,Fe)Si dispersoids can also be observed in the SEM images (Fig.1). Obviously, the number density of dispersoids in BH is much higher while their size is much smaller than in sample BL. Precipitate free zones (PFZs) around dendrite and grain boundaries were observed in AL and BL. The area fraction of PFZs in BL was ~40%, determined by the manual point count procedure of SEM images (according to ASTM E562-08). The number density of dispersoids was measured by SEM, and the volume fractions of dispersoids were calculated according to [22], as shown in Table 2. The volume fractions in BL and AL include the PFZs. The dispersoid spacing excluding PFZs, L_d, from center to center, was calculated as [6]:

$$L_d = d\sqrt{\frac{\pi}{6V_V}}. \quad (2)$$

The dispersoid size distribution fits a lognormal distribution, as shown in Fig. 1d.

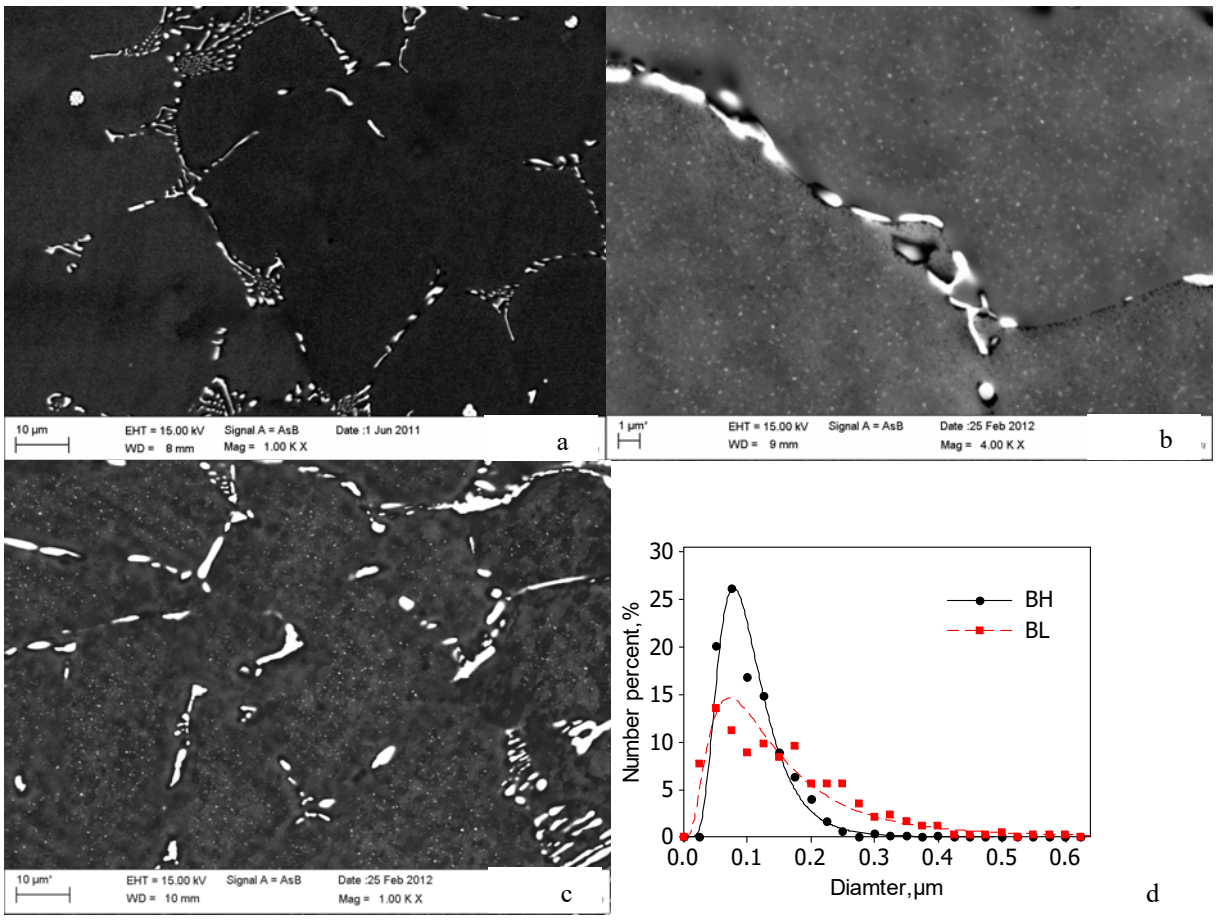

Fig.1 Back-scattered electron images of BH and BL and their size distribution of dispersoids. (a) shows the distributions of the constituent particles in BH; (b) shows the distribution of dispersoids in BH at a higher magnification; (c) shows the non-uniform distributions of constituent particles and dispersoids in BL; d) the size distribution of dispersoids in BH and BL with lognormal fitting curves.

3.2 Microstructure after tensile deformation

Figure 2 shows the dislocation structures of samples BH and BL at a tensile strain of 16%. The influence of dispersoids on the dislocation structure evolution can be clearly seen by comparing sample BH (Fig. 2a) and BL (Fig. 2b). In sample BH, a large amount of relatively loose dislocation tangles have formed around the dispersoids, forming dislocation networks. Most of the dislocation networks are connected to cell walls. In comparison to the sample BH, the dislocation density is lower while the cell size is larger in BL.

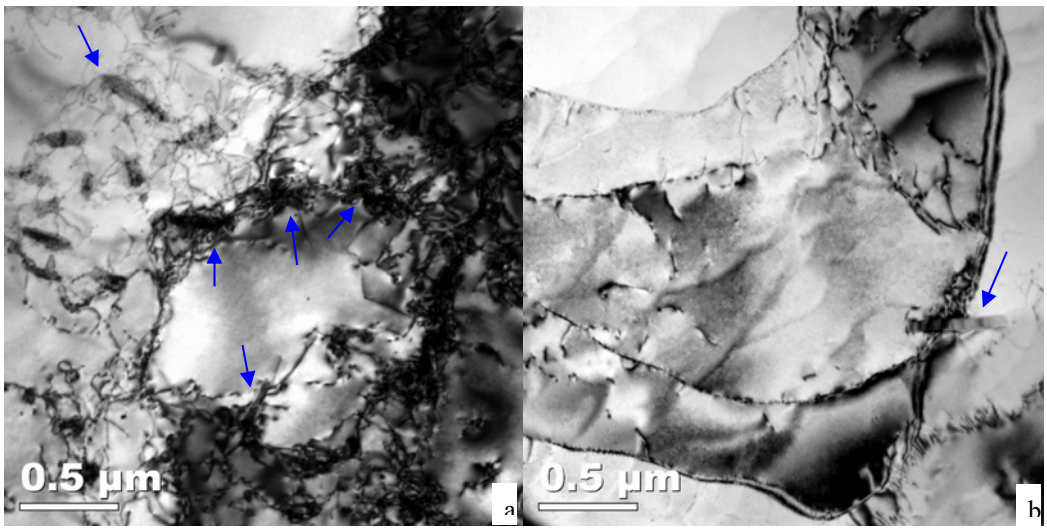

Fig. 2 TEM bright field images of the cross sections of BH (a) and BL (b) at 16% tension strain. Cell walls formed by connecting dislocation networks around dispersoids (indicated by the arrows).

The average cell size was measured from TEM images. Two orthogonal diameters, d_1 and d_2, were measured for each cell. The cell size is calculated as the square root of $d_1 \times d_2$. An average cell size is obtained by 50-70 measurements of cells. The cell sizes of sample BH and BL at 16% tensile strain are listed in Table 3. The cell sizes of sample AH and AL were 0.92 μm and 1.03 μm respectively, which are close to their interspacing of dispersoids (Table 2). The cell size of the sample containing a high-density of dispersoids was smaller than those containing a low-density of dispersoids, and the difference in cell size was statistically significant according to the Student's one-tailed t-test (significance level =0.01 for BH and BL).

3.3 Microstructure after cold rolling

The subgrain structure formed during cold rolling is shown in Figure 3. The subgrains are elongated along the rolling direction. The average subgrain sizes parallel and perpendicular to the elongation direction of subgrains were measured by lineal intercept procedures in SEM images. The number of subgrains intercepted by one straight line is about 10~40, and two or three measurements were done in each area to give an average value of both d_x and d_y. The square root of $d_x \times d_y$ is taken as the 2D subgrain size. Thus, the subgrain size measured by SEM may be not quantitatively comparable to the cell size measured by TEM. The standard deviation was based on three or four areas measured for each sample, and indicates the uniformity of subgrain structure between different grains, not the individual measurement deviation.

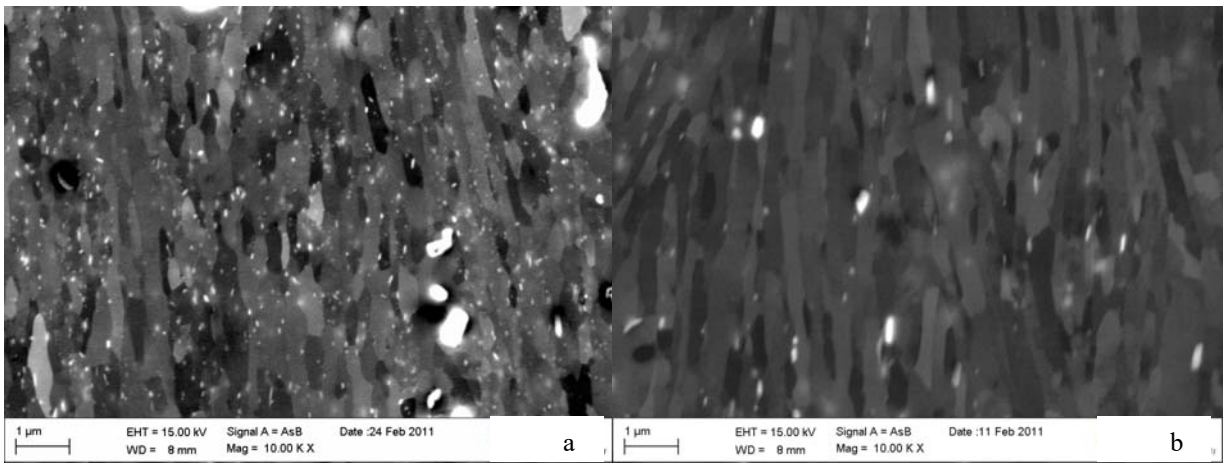

Fig.3 SEM backscattered electron images of subgrain structure and dispersoids of sample BH (a) and BL (b) at a strain of 3.3. The images were taken in the ND-RD section.

As can be seen in Table 3, the subgrain size deviation of BL at a strain of 0.74 was relatively large, indicating a non-uniform subgrain structure. BL contains ~40% PFZs, in which the evolution of subgrain structure at small strains may be different from those containing dispersoids. At larger strains, the subgrain structure appears uniform, as shown in Fig.3, consistent with the small standard deviations in Table 3. Deformation zones around constituent particles contained smaller subgrains, which were also observed, but they were not counted and considered in this work. The subgrain structures of both BH and BL were similar at large strains. The subgrain size decreases with increasing rolling strain, and the mean subgrain sizes of BH and BL are similar when the deformation strain exceeds 0.74, indicating that dispersoids do not have a significant influence on the subgrain size at large strains.

Table.3 The cell/subgrain sizes (µm) during tension or rolling.

von Mises strain	0.16	0.74	1.8	3.3
BH	0.85±0.28	1.10±0.01	0.49±0.04	0.42±0.01
BL	1.01±0.29	0.96±0.39	0.50±0.05	0.46±0.04

*The cell/subgrain size and standard deviation are defined in the text. The differences in the methods and definitions have also been noted in the text.

At large strains the dispersoids were observed mainly at subgrain boundaries. The number fraction of dispersoids located at the subgrain boundaries was estimated from the BSE-ECC images (e.g. Fig.3). The number fractions of dispersoids at subgrain boundaries at strains of 1.8 and 3.3 were ~80% in BH, and ~90% in BL. Most of dispersoids are located at subgrain boundaries in both materials at large strains. The number fraction is roughly estimated, because some of the subgrain boundaries with small misorientations can not be identified in BSE-ECC images due to the limited resolution of BSE-ECC imaging and the unfavorable orientations of some subgrains. Dispersoids reflect more back-scattered electrons and have higher contrast than aluminum matrix, so the

observed dispersoids can be deep beneath the surface while only the trace of subgrain boundaries at the surface can be observed. It is also possible that a dispersoid not at subgrain boundaries was observed at subgrain boundaries because of projection. Thus, the value of the number fraction is just roughly estimated.

3.4 Strength and work hardening

The stress-strain curves from tensile tests of as-homogenized materials are shown in Fig.4. At the initial deformation stage (strain <0.02), a smaller dispersoid spacing led to a higher flow stress as well as a higher work hardening rate. The yield strength of BH is much larger than that of BL. The 0.02% offset yield strength of BH and BL was 37 MPa and 24 MPa, respectively. The 0.2% offset yield strength of BH and BL was 56 MPa and 37 MPa, respectively. The work hardening of BH in the range of 0.02% to 0.2% plastic strain is ~19 MPa, much larger than that of BL (~13MPa). This also indicates a higher work hardening rate due to a high density of dispersoids.

The ultimate tensile strength (UTS) of as-rolled materials was plotted as a function of the von Mises strain in Fig.4. The trend lines connecting stress-strain curves of as-homogenized materials and the UTS of rolled materials indicate the work hardening behavior at large strains. The flow stresses of BH and BL approach each other with increasing strain, and finally converge at large strains, although the initial yield stresses are quite different. The Taylor factors were calculated from textures measured by X-ray diffraction. The Taylor factors of BH and BL were similar at the same strain. The Taylor factors of both samples under uniaxial tension along RD did not change at strains less than 0.74 and they increased slowly from 3.1 to 3.2 at larger strains for both BH and BL. The convergence of the stress-strain curves of BH and BL at large strains (Fig.4) indicates that the influence of dispersoids on flow stress diminished at large strains. The Vickers hardness (HV) of AH and AL is also plotted in Fig. 4, illustrating that the hardness curves of AH and AL have converged at strain of 0.4. The standard deviation of HV measurements is less than 3% of HV.

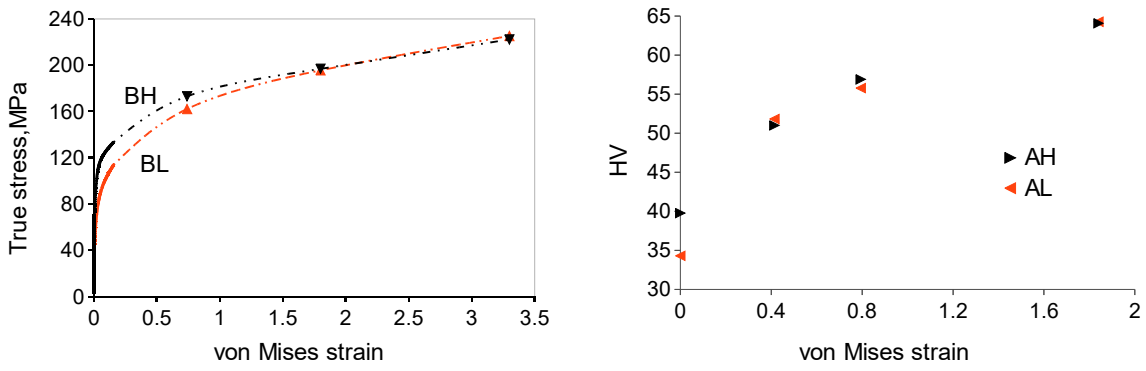

Fig.4 (a)Stress-strain curves of as-homogenized BH and BL (solid lines) and the ultimate tensile strength of materials rolled to various logarithmic strains (▼: BH, ▲: BL) (dashed lines are trend lines);(b) Vickers hardness (HV) of AH and AL in as-homogenized and rolled conditions.

3.5 Bauschinger effect

Pile-up of Orowan loops around non-shearable particles leads to an elastic internal stress, which is often referred as kinematic hardening. Internal stress due to particles may play an important role in plastic deformation of dispersion hardened materials, which can be observed during reversed strain paths, e.g. Bauschinger tests. The Bauschinger effect is illustrated in Fig.5, and compared to monotonic loading. The specimen was first deformed in tension to a prescribed forward plastic strain, and then the deformation was reversed in compression. The specimen started to buckle at 1-2% compression strain. The opposite case with prestrain of ~1% in compression and then tension tested in Fig.5 shows that the reverse stress approaches the monotonic curve, converging at a strain of ~0.1. The convergence suggests that the reduced strength after the reversal is not permanent.

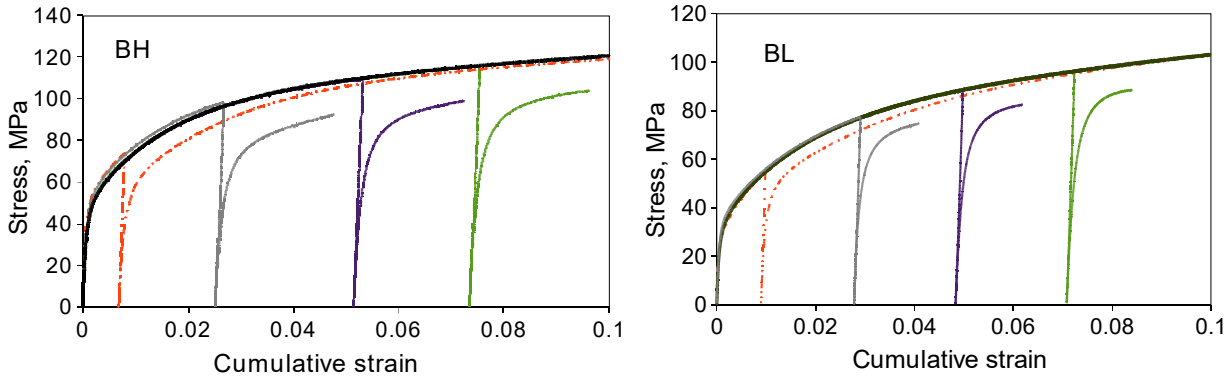

Fig.5 Forward-reverse stress -cumulative strain curves following different forward plastic strains. Solid lines: tension-compression; dashed lines: compression-tension tests.

As previously suggested in [20, 24-25], the Bauschinger stress is defined to equal half of the difference between the monotonic and the reversed stress-strain curves. The Bauschinger stress obtained from Fig.5 is shown in Fig.6. The Bauschinger stress curve in Fig.6 is comprised of two parts: firstly a rapid reduction at small reverse strains (<0.004); secondly a regime where the Bauschinger stress decreases slowly in a nearly linear manner with increasing strain. The first part involves inhomogeneous local stresses and complex dislocation rearrangements [25-26], which is not further considered in present work. The subsequent regime indicates an almost steady-state Bauschinger stress. The Bauschinger stress at the reverse strain of 1% is used as the "steady-state" internal stress σ_b. The results are shown in Fig.7. The internal stress increases with increasing plastic strain, and it starts to saturate at a strain of ~5%.

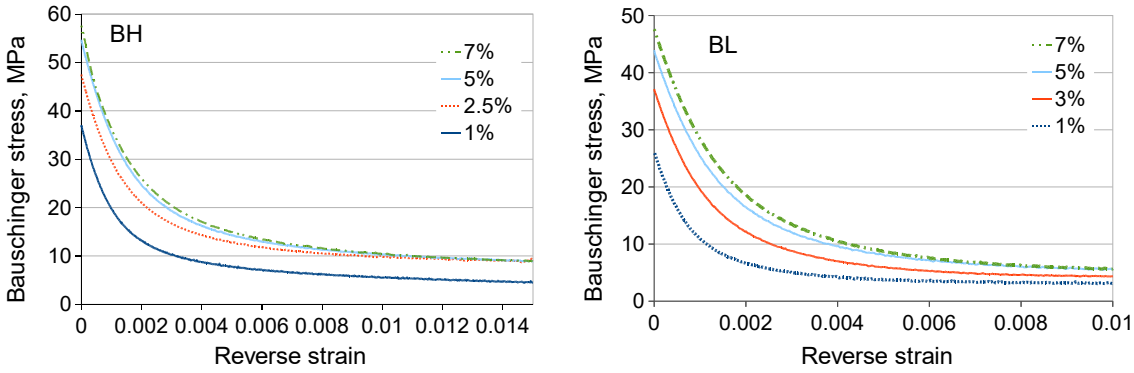

Fig.6 Bauschinger stress as a function of reverse strain.

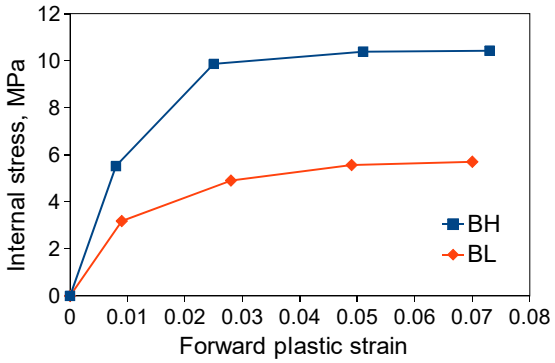

Fig.7 Evolution of internal stress as a function of the forward plastic strain.

4. Discussion

4.1 Influence of dispersoids on the evolution of the cell structure

A cell structure forms during deformation as the result of trapping and annihilation of dislocations. Dislocation loops (GNDs) form around dispersoids during deformation, in the form of Orowan loops around dispersoids, rows of prismatic loops in the vicinity of dispersoids, and dislocation helices or dipoles as well [5, 11]. The extra GNDs formed due to dispersoids result in a high local density of dislocations, providing more trapping sites for gliding dislocations. Then dislocation networks or tangles tend to form at these preferable sites. The prismatic loops emitted from adjacent dispersoids interact by trapping and annihilating each other, where the particles act as sources of GNDs that contribute to the building of new cell walls. New cell walls can form by connecting the fragments of dislocation tangles, as indicated by TEM observations in Fig. 2. The dispersoids and GNDs promote cell wall formation, leading to reduced cell sizes at small strains, which is observed in this work (Table 3) and also reported before [9, 12]. It is concluded that the magnitude of the reduction of cell size is related to the dispersoid spacing (or density), i.e. the smaller dispersoid spacing, the smaller cell size. However, when the dispersoid spacing is very small, the density of GNDs and the additional dislocations may be so high that the dislocation distribution appears uniform in the matrix. Then the formation of cell walls by heterogeneously trapping gliding

dislocations would be suppressed. Thus, the mechanism of reducing the cell size by dispersoids would not be effective when the dispersoid spacing is very small. It has been observed that cell formation is retarded in an Al-Sc alloy with a dispersoid spacing of 100 nm [27].

The effect of dispersoids on cell formation also changes with the deformation strain. As the strain increases, the cell size becomes smaller. When the cell size is reduced to a smaller size than dispersoids spacing, the effect of dispersoids on cell formation diminishes. As can be seen in Table 3, the subgrain sizes of BH and BL are both found to be similar, ~0.5 μm at strains larger than 1.8, which is smaller than the dispersoid spacing (0.9-1.4 μm in Table 2). Hansen and Bay [28] also found that neither the content nor the distribution of fine dispersed particles (0.6-1.2 wt% Al_2O_3) affected the subgrain size significantly after 50-90% drawing. The evolution of subgrains at large strains seems to be independent of the dispersoid spacing as the subgrain size becomes smaller than dispersoid spacing.

4.2 Yield strength

The coarse constituent particles distributed on dendrite and grain boundaries in the as-cast materials are of a low number density and large in size, so their contribution to dispersion hardening by Orowan bypass mechanism is negligible. The Orowan stress is mainly due to the fine dispersoids. Thus, the yield strength is given by:

$$\sigma_y = \sigma_0 + \sigma_{SS} + \sigma_{HP} + \sigma_{Oro}. \quad (3)$$

σ_0 is the friction stress of pure aluminum. σ_{SS} is solid solution hardening, for which an empirical relation for Al-Mn can be found in [29]. σ_{HP} is the Hall-Petch relation of the grain size effect given by [30]. Both σ_{SS} and σ_{HP} do not affect the comparison between BH and BL, since their solute contents and grain sizes are similar. σ_{Oro} is the Orowan stress due to fine dispersoids, which is given by

$$\sigma_{Oro} = 0.81\frac{MAGb}{2\pi\lambda}\ln\left(\frac{\pi d}{4b}\right). \quad (4)$$

The equation is given by [13]. M is the Taylor factor (M≈3 here); G is the shear modulus of aluminum (G=27MPa); b is Burgers vector (b=0.286nm). A is a constant, which is treated as a fitting parameter here. $\lambda = 0.4d\left(\sqrt{\pi / f_V} - 2\right)$ is the dispersoid spacing (surface to surface) on a slip plane, [6]. f_V and d are the volume fraction and diameter of dispersoids, respectively. The difference in yield stress between BH and BL is contributed by the Orowan stress, and then the value of A is estimated by fitting the calculations to the experimental results. A becomes 1.2 by fitting to 0.02% yield strength, and is 1.8 by fitting to 0.2% yield strength. The value of A can also

be estimated by $A = 1/\sqrt{1-\nu}$ given in [13] (where ν=0.34 is Poisson's ratio), and then equals 1.2. The dispersion-hardened material has a significantly higher initial work hardening rate than the matrix material. Thus, the fitted value of A increases with increased offset strain. To reduce the influence of initial work hardening, the offset of yield strength should be as small as possible.

4.3 Bauschinger effect

Generally, the internal stress due to particles can be expressed based on Eshelby's solution [20] as

$$\sigma_b = f_p E_p \varepsilon^* \quad (5)$$

E_p is the Young's modulus of particles, and f_p is the volume fraction of particles. ε^* is the unrelaxed plastic strain and $\varepsilon^* \propto n/r$ [19], where n is the number of Orowan loops hugging the particles and r is their radius. This implies that the smaller size of dispersoids in BH will lead to a larger internal stress. There is a large fraction of constituent particles in the alloy, which is much larger than the fraction of dispersoids (Table 2). These coarse constituent particles might produce a tangle of secondary dislocations instead of Orowan loops, inducing a weaker internal stresses than Orowan loops [18, 31].

There are two types of particles in the alloy regardless being constituent particles or dispersoids: Al_6(Mn,Fe) and α-Al(Mn,Fe)Si. It is reported that the chemical composition of particles changes during homogenization and that the fraction of α-Al(Mn,Fe)Si particles increases [23]. This probably results in different Young's modulus for the particles in BH and BL. The shape of coarse constituent particles is not regularly spherical or plate-like, and their shapes also change during homogenization. Therefore a quantitative comparison of internal stress according to Eq. (5) is difficult. A qualitative assessment of the contribution of the internal stress is attempted in the present work. The ratio of the internal stress to the monotonic flow stress at the same total strain is in the range of 5% to 10% in BH and BL at forward plastic strain of 1-5%. The contribution of the internal stress to the total work hardening is estimated as $\sigma_b/(\sigma_F - \sigma_y)$, following the method used in [20]. Here σ_F is the forward flow stress at the point of reversal, and σ_y is the 0.02% yield stress. The ratio is shown as a function of forward plastic strains in Fig.8. It increases rapidly at a small strain $\leqslant$1%, and from there it contributes ~16% and 10% in BH and BL respectively. The internal stress due to particles plays a minor role in work hardening after the initial stage, and this contribution is small compared to more than 40% in the overaged alloys in [20].

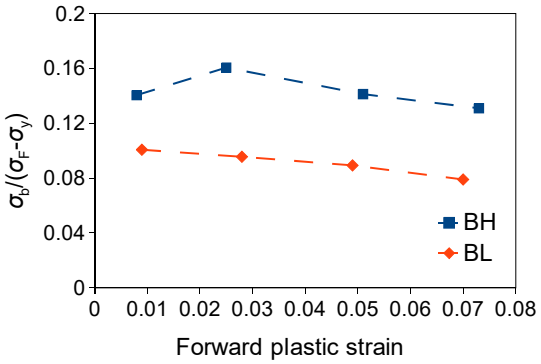

Fig. 8 The ratio of the internal stress to the total work hardening as a function of the forward plastic strain.

4.4 Strengthening at small strains

The flow stress at small strains is assumed to be:

$$\sigma = \sigma_0 + \sigma_{SS} + \sigma_{HP} + \sigma_{Oro} + \sigma_i + \sigma_b = \sigma_y + \sigma_i + \sigma_b . \quad (6)$$

It is noted that a non-linear superposition of the hardening components has been discussed before [32-34]. The linear assumption is used for the sake of simplicity in the present work. Isotropic stress σ_i corresponds to the contribution of dislocation interactions: $\sigma_i = M\alpha Gb\sqrt{\rho}$, where α is a constant. The total dislocation density, ρ, includes statistically stored dislocations (i.e. forest dislocations), ρ_S, and GNDs, ρ_G: $\rho = \rho_S + \rho_G$. Many models have been proposed for the evolution of forest dislocations and they will not be discussed in this work. The evolution of GNDs is often modeled following Ashby's approach [19]. The magnitude of the isotropic hardening can be estimated from $\sigma_F - \sigma_y - \sigma_b$ as shown in Fig. 9. The difference between BH and BL in Fig. 9 is caused by the GND density due to the different densities of dispersoids. The maximum difference between σ_i for BH and BL is ~7MPa, similar to the difference between their saturated internal stresses in Fig.7. It indicates that the magnitude of the contribution of GNDs to the flow stress is similar as from the internal stress. In Fig. 9 the isotropic stress of BL approaches that of BH at strains larger than 0.08. This is probably caused by a stronger dynamic recovery in BH. A high density of dispersoids induces additional dislocations, and also accelerates dynamic recovery, as suggested in [34].

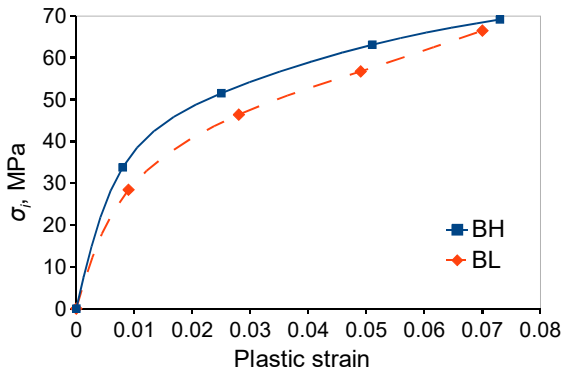

Fig.9 The calculated isotropic stress ($\sigma_i = \sigma_F - \sigma_y - \sigma_b$) as a function of plastic strain.

The internal stress in principle is a long-range elastic stress from dislocation pile-ups at boundaries or particles. The contribution from the boundaries has been included in the Hall-Petch relation. The internal stress due to particles is found to saturate at a certain tensile strain (usually <8%), which is shown in Fig.7 and Ref. [20-21]. Thus, the internal stress does not contribute to the work hardening rate after its saturation and its contribution to the total work hardening becomes minor at moderate and large strains. Moreover, the formation of deformation zones around coarse particles relieves the internal stress from the coarse particles as well. Thus, internal stress could be neglected at moderate and large strains. Work hardening at large strains is mainly attributed to the dislocation interactions.

4.4 Strengthening at large strains

At large strains, e.g. during rolling, the dislocation density inside subgrains has saturated, and the flow stress scales inversely with the subgrain size [35]. As discussed in section 4.1, the subgrain size is found not to be affected by dispersoids at large strains (Table 3). Thus, all the stress components except the Orowan stress are not affected by dispersoids at large strains. The equal flow stresses of BH and BL at large strains suggest that the Orowan stress is absent at large strains. The Orowan stress is based on the bow out of gliding dislocation between dispersoids. Most of the dispersoids are tangled in subgrain boundaries or triple junctions at large strains, as shown in section 3.3, so the major barriers to gliding dislocations are grain/subgrain boundaries containing dispersoids and these barriers should only be counted once. Thus, the Orowan stress can be neglected comparing to the boundary strengthening. Then the flow stress of alloys containing dispersoids will approach to the single-phase alloys. The strain at which the stress-strain curves converge depends on dispersoid density (or spacing). The high dispersoid density (small spacing) is expected to lead to a convergence upon large strains. This is verified by the convergence of AH and AL at smaller strain due to their lower density of dispersoids, as shown in Fig. 4. The flow stress after the convergence is affected by the solute content, not the dispersoids. The dispersion hardening

is not effective at large strains.

5. Summary

A high density of fine dispersoids has been shown to strengthen the materials significantly, but their strengthening effect diminishes as the strain increases. The internal stress due to particles makes a contribution to the total work hardening (i.e. 10-20%) and starts to saturate at a tensile strain of 3-5%, although it increases rapidly at the initial stage of the deformation. The dislocation interactions, i.e. forest hardening, play a major role in the subsequent work hardening. Geometrically necessary dislocations which are formed around dispersoids, enhance the formation of cell structure and lead to a reduced cell size. The dispersoids tend to be trapped in cell walls or subgrain boundaries. When the cell/subgrain size becomes smaller than the dispersoid spacing, the dispersoids do not affect the subgrain size and do not contribute to the strength any more. The flow stress is dominated by the substructure at moderate and large strains.

Acknowledgement

The authors are grateful for the assistance of Ning Wang and Pål Christian Skaret with SEM observations and tensile tests respectively. This work was funded by Research Council of Norway, Hydro and Sapa Technology under the project MOREAL.

References

[1] Y.J. Li, A.M.F. Muggerud, A. Olsen, T. Furu, Acta Mater., 60 (2012) 1004-1014.
[2] M.F. Ashby, Philos Mag, 14 (1966) 1157-1178.
[3] M.H. Lewis, J.W. Martin, Acta Metall., 11 (1963) 1207-1214.
[4] P. Hirsch, F. Humphreys, Proc. R. Soc. London, A, 318 (1970) 45-72.
[5] F. Humphreys, P. Hirsch, Proc. R. Soc. London, A, 318 (1970) 73-92.
[6] N. Hansen, Acta Metall., 18 (1970) 137-145.
[7] J.D. Embury, W.J. Poole, D.J. Lloyd, Mater. Sci. Forum, 519-521 (2006) 71-78.
[8] B. Forbord, K. Marthinsen, E. Nes, Mater. Sci. Forum, 331-337 (2000) 557-564.
[9] C.Y. Barlow, N. Hansen, Acta Metall., 37 (1989) 1313-1320.
[10] C.Y. Barlow, N. Hansen, Y.L. Liu, Acta Mater., 50 (2002) 171-182.
[11] F.J. Humphreys, A.T. Stewart, Surf. Sci., 31 (1972) 389-421.
[12] D.J. Lloyd, D. Kenny, Acta Metall., 28 (1980) 639-649.
[13] L.M. Brown, R.K. Ham, Dislocation-particle interactions, in: A. Kelly, R.B. Nicholson (Eds.) Strengthening Methods in Crystals, Elsevier, Amsterdam, 1971, pp. 9-135.
[14] B. Reppich, Particle Strengthening, in: R.W. Cahn, P. Haasen, E.J. Kramer (Eds.) Materials science and technology: a comprehensive treatment, Wiley-VCH, Weinheim, 2005, pp. 311.
[15] V. Gerold, Precipitation hardening, in: F.R.N. Nabarro (Ed.) Dislocations in solids, North-Holland, New York, 1979, pp. 219-260.
[16] J.C. Fisher, E.W. Hart, R.H. Pry, Acta Metall., 1 (1953) 336-339.
[17] L.M. Brown, W.M. Stobbs, Philos Mag, 23 (1971) 1185-1199.
[18] L.M. Brown, W.M. Stobbs, Philos Mag, 23 (1971) 1201-1233.
[19] M.F. Ashby, Philos Mag, 21 (1970) 399-424.

[20] H. Proudhon, W.J. Poole, X. Wang, Y. Bréchet, Philos Mag, 88 (2008) 621-640.
[21] G. Fribourg, Y. Bréchet, A. Deschamps, A. Simar, Acta Mater., 59 (2011) 3621-3635.
[22] Y.J. Li, L. Arnberg, Acta Mater., 51 (2003) 3415-3428.
[23] Y.J. Li, L. Arnberg, Mater. Sci. Eng., A, 347 (2003) 130-135.
[24] D.V. Wilson, Acta Metall., 13 (1965) 807-814.
[25] J.D. Atkinson, L.M. Brown, W.M. Stobbs, Philos Mag, 30 (1974) 1247-1280.
[26] W.Z. Han, A. Vinogradov, C.R. Hutchinson, Acta Mater., 59 (2011) 3720-3736.
[27] P.J. Apps, M. Berta, P.B. Prangnell, Acta Mater., 53 (2005) 499-511.
[28] N. Hansen, B. Bay, J. Mater. Sci., 7 (1972) 1351-1362.
[29] Ø. Ryen, O. Nijs, E. Sjölander, B. Holmedal, H.E. Ekström, E. Nes, Metall. Mater. Trans. A, 37 (2006) 1999-2006.
[30] N. Hansen, Acta Metall., 25 (1977) 863-869.
[31] L.M. Brown, W.M. Stobbs, Philos Mag, 34 (1976) 351-372.
[32] U.F. Kocks, A.S. Argon, M.F. Ashby, Prog. Mater. Sci., 19 (1975) 1-281.
[33] Y. Dong, T. Nogaret, W.A. Curtin, Metall. Mater. Trans. A, 41 (2010) 1954-1960.
[34] J. da Costa Teixeira, L. Bourgeois, C.W. Sinclair, C.R. Hutchinson, Acta Mater., 57 (2009) 6075-6089.
[35] E. Nes, Prog. Mater. Sci., 41 (1997) 129-193.